The Astrophysical Journal, 931:125 (8pp), 2022 June 1 https://doi.org/10.3847/1538-4357/ac6a57

Constraints on Cosmic Rays in the Milky Way Circumgalactic Medium from O VIII Observations

Manami Roy and Biman B. Nath
Raman Research Institute, Sadashiva Nagar, Bangalore 560080, India; manamiroy@rri.res.in
Received 2022 January 4; revised 2022 April 11; accepted 2022 April 22; published 2022 June 2

Abstract

We constrain the cosmic-ray (CR) population in the circumgalactic medium (CGM) of the Milky Way by comparing the observations of absorption lines of O VIII ions with predictions from analytical models of the CGM: the precipitation (PP) and isothermal (IT) models. For a CGM in hydrostatic equilibrium, the introduction of CR suppresses thermal pressure and affects the O VIII ion abundance. We explore the allowances given to the ratio of CR pressure to thermal pressure ($P_{\rm CR}/P_{\rm th}=\eta$), with varying boundary conditions, CGM mass content, photoionization by extragalactic ultraviolet background, and temperature fluctuations. We find that the allowed maximum values of η are $\eta \lesssim 10$ in the PP model and $\eta \lesssim 6$ in the IT model. We also explore the spatial variation of η: rising ($\eta = Ax$) or declining ($\eta = A/x$) with radius, where A is the normalization of the profiles. In particular, the models with a declining ratio of CR to thermal pressure fare better than those with a rising ratio with suitable temperature fluctuation (higher $\sigma_{\rm lnT}$ for PP and lower for IT). The declining profiles allow $A \lesssim 8$ and $A \lesssim 10$ in the case of the IT and PP models, respectively, thereby accommodating a large value of η ($\simeq$200) in the central region but not in the outer regions. These limits, combined with the limits derived from the γ-ray and radio background, can be useful for building models of the Milky Way CGM including the CR population. However, the larger amount of CRs can be packed in the cold phase, which may be one way to circumvent these constraints.

Unified Astronomy Thesaurus concepts: Cosmic rays (329); Circumgalactic medium (1879)

1. Introduction

Galaxies have two components: a galactic disk surrounded by a gaseous and a dark matter halo. The gaseous halo, which extends up to the virial radius (sometimes even beyond), is known as the circumgalactic medium (CGM). It is a reservoir for most of the baryons and plays a crucial role in galaxy formation and evolution by various feedback processes such as outflowing and recycling of gas (Tumlinson et al. 2017). Soft X-ray observation of O VII and O VIII absorption (Gupta et al. 2012; Fang et al. 2015) and emission lines (Henley & Shelton 2010; Henley et al. 2010) and the Sunyaev-Zel'dovich (SZ) effect (Planck Collaboration et al. 2013; Anderson et al. 2015) indicate the presence of a hot phase ($T \geqslant 10^6$ K) of the CGM. Recently, a warm (10^5 K $< T < 10^6$ K) and a cool phase (10^4 K $< T < 10^5$ K) of the CGM have also been discovered through absorption lines of low and intermediate ions[1] (Tumlinson et al. 2017) at low redshifts (Stocke et al. 2013; Werk et al. 2014, 2016; Prochaska et al. 2017) and Lyα emission at high redshifts (Hennawi et al. 2015; Cai et al. 2017). It is not yet clear how this cool phase coexists with the hot phase and survives the destructive effects of various instabilities (McCourt et al. 2015; Ji et al. 2018), but this discovery has led to a picture of multiphase temperature and density structure of the CGM (Tumlinson et al. 2017; Zhang 2018). It also partially solves the problem of missing baryons in the galaxies (Tumlinson et al. 2017).

If the CGM is considered to be in hydrostatic equilibrium by means of only thermal pressure, then in order to maintain pressure equilibrium, the cold component ($\sim 10^4$ K) of the CGM is expected to have a higher density than the hot component ($\sim 10^6$ K). However, Werk et al. (2014) found the density of cold gas to follow the hot gas density distribution. This has given rise to the idea of a nonthermal pressure component, consisting of cosmic-ray (CR) and magnetic pressure, which can add to the thermal pressure. Without a nonthermal component, the abundances of low and intermediate ions (seen in cool and warm phases, respectively) are underestimated even in high-resolution simulations (Hummels et al. 2019; Peeples et al. 2019; van de Voort et al. 2019). Ji et al. (2020) have suggested that CRs can explain these two problems. It has been suggested that CRs can provide pressure support to cool diffuse gas (Salem et al. 2015; Butsky & Quinn 2018), help in driving galactic outflows (Ruszkowski et al. 2017; Wiener et al. 2017), and excite Alfvén waves that can heat the CGM gas (Wiener et al. 2013).

The magnitude of the CR population in the CGM is, however, highly debated. Some simulations (Butsky & Quinn 2018; Dashyan & Dubois 2020; Ji et al. 2020) claimed a CR-dominated halo, which increases feedback efficiency of the outflowing gas by increasing the mass loading factor and suppressing the star formation rate. The ratio of CR pressure and thermal pressure ($P_{\rm CR}/P_{\rm th}=\eta$) controls this effect and can reach a large value exceeding 10 over a huge portion of a Milky Way (MW) sized halo (Butsky & Quinn 2018). Another simulation claimed that an MW-sized halo at low redshift ($z < 1$) can be CR populated with η nearly 10 in outflow regions, although in warm regions ($T = 10^5$ K) of the halo $\eta \leqslant 1$ (Ji et al. 2020). Dashyan & Dubois (2020) found in their simulation that dwarf galaxies, with virial mass 10^{10}–$10^{11}\,M_\odot$, can have a high value of η ($\sim$100) at 1–5 kpc from the

[1] Low ions: ionization potential (IP) < 40 eV, $T = 10^{4-4.5}$ K; intermediate ions: $40 \gtrsim$ IP (eV) $\lesssim 100$, $T = 10^{4.5-5.5}$ K; high ions: IP $\gtrsim 100$, $T > 10^{5.5}$ K.

midplane when isotropic diffusion is incorporated (their Figures 1 and 2).

It is therefore an important question as to how many CRs can be accommodated in the CGM in light of different observations. One of the most obvious effects of the CR population in the CGM is to suppress the thermal pressure of the hot phase, which is also seen in the simulation of Ji et al. (2020). The recent work by Kim et al. (2022) pointed out that this reduction in thermal pressure would lower the thermal SZ (tSZ) signal, as tSZ probes the integrated thermal pressure in the halo. This diminished value of thermal pressure would also significantly change the abundance of high ionization species and thereby jeopardize the interpretation of their column densities. In a recent work by Faerman et al. (2022), they modified their previous isentropic model (Faerman et al. 2020) with significant nonthermal pressure ($\alpha = (P_{\rm nth}/P_{\rm th}) + 1.0 = 2.9$) and found that the gas temperature in the central region for the nonthermal model becomes lower than the value at which O VIII collisional ionization equilibrium temperature peaks, which in turn results in a lower O VIII column density. At low CGM masses, photoionization compensated for this effect by the formation of O VIII at larger radii, but for large gas masses and large mean densities (as in the MW), the photoionization effect is negligible and the total O VIII column density is low. In a previous work (Jana et al. 2020), we constrained the CR pressure ($\eta = P_{\rm CR}/P_{\rm th}$) in the CGM in light of the isotropic γ-ray background (IGRB) and radio background, using different analytical models (isothermal model: IT; precipitation model: PP) of the CGM. In the case of the IT model, the value of IGRB flux puts an upper limit of 3 on η, whereas all values of η are ruled out if one considers the anisotropy of the flux due to the off-center position of the solar system in the MW. However, in the case of the PP model, the IGRB flux value and its anisotropy allow a range of η from 100 to 230. In comparison, the constraints from the radio background are not quite robust. In this paper we use the same analytical models (IT and PP) and put limits on the CR population in the CGM of the MW by comparing the predicted O VIII absorption column densities ($N_{\rm O\ VIII}$) with the available observations.

It might still be asked, why use O VIII as a probe? Previous works (Faerman et al. 2017; Roy et al. 2021) explained the observed O VII and O VIII absorption column densities in the MW without the incorporation of the CR component using the analytical models of the CGM used here. It is therefore important to study the effect of CRs on these column densities with the inclusion of the CR component in these models. Whereas the O VII ion has a plateau of favorable temperatures (5×10^5 K to 1×10^6 K), the suitable temperature for O VIII production (2×10^6 K) peaks near the temperature of the hot halo gas of the MW CGM. This particular fact makes O VIII abundance a sensitive probe of the CGM hot gas and motivates the choice of O VIII column density for comparison with the observations in order to constrain the CR population in the MW CGM.

2. Density and Temperature Models

We study two widely discussed analytical models: IT and PP. These models have previously been studied in the context of absorption and emission lines from different ions (Faerman et al. 2017; Voit 2019; Roy et al. 2021) We assume the CGM to be in hydrostatic equilibrium within the potential of the dark matter halo ($\phi_{\rm DM}$), with a metallicity of 0.3 $Z_\odot$ (Prochaska et al. 2017), so that

$$\frac{dP_{\rm total}}{dr} = -\frac{d\phi_{\rm DM}}{dr}\rho, \tag{1}$$

where $P_{\rm total}$ is the total pressure and ρ and r are the density and radius, respectively. We consider the Navarro–Frenk–White (NFW; Navarro et al. 1996) profile as the underlying dark matter potential in the IT model. However, we slightly modify this potential in the case of the PP model as suggested in Voit (2019) by considering the circular velocity (v_c) to be constant ($v_{\ c,\rm max} = 220\ \rm km\ s^{-1}$) up to a radius of 2.163 $r_{\rm vir}/c$ for a halo with $M_{\rm vir} = 2 \times 10^{12}\ M_\odot$ and concentration parameter $c = 10$. We include nonthermal pressure support with the CR population and magnetic field along with thermal pressure in these models. We consider the magnetic energy to be in equipartition with thermal energy ($P_{\rm mag} = 0.5\, P_{\rm th}$) so that the total pressure $P_{\rm total} = P_{\rm th}(1.5 + \eta)$, which leads to

$$\frac{dT}{dr} = -\left(\frac{1}{1.5 + \eta}\right)\left(\frac{\mu m_p}{k}\right)\frac{d\phi_{\rm DM}}{dr} - \left(\frac{T}{n}\right)\frac{dn}{dr}. \tag{2}$$

Note that the magnitude of magnetic field in the CGM is rather uncertain. While Bernet et al. (2008) claimed that the magnetic field in the CGM of galaxies at $z = 1.2$ is larger than that in present-day galaxies, the observations of Prochaska et al. (2019) suggested a value less than that given by equipartition. Yet another study claimed a near-equipartition value after correlating the rotation measures of high-z radio sources with those in the CGM of foreground galaxies (Lan & Prochaska 2020).

The inclusion of nonthermal pressure suppresses the thermal pressure, and in turn the temperature or density, or both, of the CGM gas (also seen in recent simulations of Ji et al. 2020). Our goal is to determine the effect of the inclusion of the CR population on $N_{\rm O\ VIII}$ and therefore constrain the CR population in the MW CGM. In addition to models with uniform η, we have studied the effect of varying η as a function of radius. For this, we have explored two contrasting variations, $\eta = A \times x$ (rising profile) and $\eta = A/x$ (declining profile), where $x = r/r_s$ and A is the normalization of the profiles. We primarily studied the case with $A = 1$, where the maximum value (for $\eta = x$) is $r_{\rm vir}/r_s = {\rm c} = 10$. For $\eta = 1/x$, to avoid divergence at $r = 0$ kpc, we have started our calculation from $r = 1$ kpc; therefore, the maximum value in this case is $r_s/1\ \rm kpc = 26$. We have shown the profiles of $\eta = x$ and $1/x$ in Figure 1. We have explored the effects of scaling up and down the values with these profiles as well (e.g., $\eta = Ax$, B/x, with A, $B \geqslant 1$). Although η can vary in a more complicated manner, we study these two particular cases (increasing and decreasing linearly) as the simplest representatives of a class of models in which η is allowed to vary with radius. It should be noted that the η here denotes the CR pressure in the diffuse hot gas with respect to thermal pressure of the hot gas.

There are several ways to proceed, starting from Equation (2). One way is to simply consider the temperature all over the CGM to be constant, which implies that the LHS of Equation (2) is zero. Another way is to use specific entropy to relate the two unknown quantities in Equation (2), temperature and density. We discuss these two ways in detail in the following subsections.

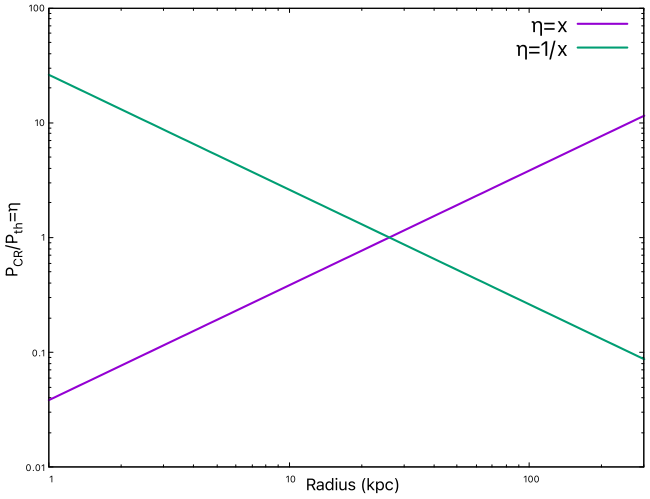

Figure 1. Radial profiles of η in the case of $\eta = x$ and $1/x$.

2.1. Isothermal Model

The IT model provides the simplest model for the CGM gas with a constant temperature, so that

$$\frac{dn}{dr} = -\left(\frac{1}{1.5+\eta}\right)\left(\frac{\mu m_p}{k\,T}\right)\frac{d\phi_{\rm DM}}{dr} \times n. \quad (3)$$

Previously hot gas has been modeled using the isothermal profile by Miller & Bregman (2015), where they fitted their model with the O VIII emission-line observations, which determined the hot gas mass to be within the range of $\sim(2.7\text{–}4.7)\times10^{10}\,M_\odot$. Therefore, we normalize the density profile isothermal model without any nonthermal component such that the hot gas mass is $5\times10^{10}\,M_\odot$. It should be noted that the single-temperature IT model does not represent the multiphase nature of the CGM. However, O VIII abundance is sensitive mostly to the hot phase of the CGM, which is well described by the single-phase model. Therefore, our limits from the IT model will not change even if we have a two- or three-temperature model. Another way of incorporating multiphase in the IT model is to consider temperature distribution around the single mean temperature. We will show below that incorporation of such a distribution in the IT model will tighten our limit on CRs. We can therefore treat the limit from our single-temperature IT model as an upper limit. We then include a nonthermal pressure component in our model along with the thermal pressure. At this point, there are again several ways to proceed. One can fix the mass and hence the density profile of the hot gas and compensate for the decrease in thermal pressure by reducing the temperature (Jana et al. 2020). Another way is to fix the temperature and reduce the density by keeping the boundary value the same. However, for massive galaxies ($M_{\rm vir}\geqslant10^{12}\,M_\odot$; Li et al. 2015), as well as the MW (Miller & Bregman 2015), the halo temperature is observed to be $\geqslant2\times10^6$ K. This motivates us to assume a constant CGM temperature of 2×10^6 K for the entire IT model (without and with nonthermal pressure; Miller & Bregman 2015). We therefore vary the density profile for different values of η by keeping the density at the outer boundary fixed. This lowers the inner density for increasing values of η, and for $\eta = 10$, the hot gas mass becomes $2.7\times10^{10}\,M_\odot$—the lower limit of hot gas mass obtained by Miller & Bregman (2015). We therefore do not consider larger values of $\eta\geqslant10$ for the IT model. In the left panel of Figure 2, density profiles for the IT model are shown by black solid ($\eta = 0$) and dotted lines ($\eta = 10$). The gray solid and dotted lines in the right panel of Figure 2 denote the $\eta = x$ and $1/x$ cases, respectively.

2.2. Precipitation Model

The PP model is a physically motivated CGM model that uses the specific entropy as a connection between density and temperature. It is built on the concept of a threshold limit for the ratio of radiative cooling time ($t_{\rm cool}$) to freefall time ($t_{\rm ff}$). Recent phenomenological studies and numerical simulations (e.g., McCourt et al. 2012; Sharma et al. 2012; Voit & Donahue 2015) showed that thermally unstable perturbations can lead to multiphase condensation below this threshold value. In this model, we consider a composite entropy profile ($K_{\rm pNFW}(r)$) with the combination of base entropy and precipitation-limited entropy,

$$K_{\rm pNFW}(r) = K_{\rm pre}(r) + K_{\rm base}(r), \quad (4)$$

where the base profile is

$$K_{\rm base} = (39\ {\rm keV\ cm^2})\ v_{200}^2\left(\frac{r}{r_{200}}\right)^{1.1} \quad (5)$$

and the precipitation-limited profile is

$$K_{\rm pre} = \left[\frac{2kT(r)}{\mu m_p v_c^2(r)}\right]^{1/3}\left\{\frac{10}{3}\left(\frac{2n_{\rm H}^2}{n_e n}\right)\Lambda_{\rm N}[T(r)]\,r\right\}^{2/3}. \quad (6)$$

Then, using $n_e = (kT/K_{\rm pNFW})^{3/2}$, it follows from Equation (2) that

$$\frac{dT}{dx} = \frac{2}{5}\left[-\left(\frac{\mu m_H}{k}\right)\frac{d\phi}{dx} + \frac{3}{2}\frac{T}{K_{\rm pNFW}}\frac{dK_{\rm pNFW}}{dx}\right]. \quad (7)$$

A recent study by Butsky et al. (2020) has shown the effect of CR pressure on thermal instability and precipitation for different values of the ratio $t_{\rm cool}/t_{\rm ff}$. In their study, they found that large CR pressure decreases the density contrast of cool clouds. In our model, we keep $t_{\rm cool}/t_{\rm ff}$ constant throughout the halo. Although observations and simulations of the intercluster medium point toward a value of this ratio between 5 and 20, it is a rather uncertain parameter in the case of CGM studies and can have a wide range. We explore a range of the temperature boundary condition ($T_{\rm bc}$) at the virial radius between $T_{\rm bc1} = 0.5\mu m_p {v_c}^2 = 1.8\times10^6$ K ($\simeq$virial temperature of the MW) and $T_{\rm bc2} = 0.25\mu m_p {v_c}^2 = 8.8\times10^5$ K (used originally by Voit 2019). The inclusion of nonthermal pressure in the model suppresses the temperature and in turn the density. However, we keep the mass of the CGM gas constant by decreasing the $t_{\rm cool}/t_{\rm ff}$ ratio. The variation of $t_{\rm cool}/t_{\rm ff}$ with η for different values of the temperature boundary condition can be seen in Figure 2 of Jana et al. (2020). We have taken the mass of the CGM to be in the range from $6\times10^{10}\,M_\odot$ (from the original model of Voit 2019 without CRs) to $2.0\times10^{11}\,M_\odot$ (for the cosmic baryon fraction) in the case of $T_{\rm bc1}$. However, the mass range for $T_{\rm bc2}$ is $6\times10^{10}\,M_\odot$ to $1.0\times10^{11}\,M_\odot$ since beyond this upper limit of mass the value of $t_{\rm cool}/t_{\rm ff}$ falls below 1. We use the cooling function from CLOUDY (Ferland et al. 2017) for a metallicity of $0.3\,Z_\odot$.

We show the temperature and density profiles for PP in Figure 2 as shaded regions, bracketing the range of CGM mass mentioned above. In the left panel of Figure 2, the temperature

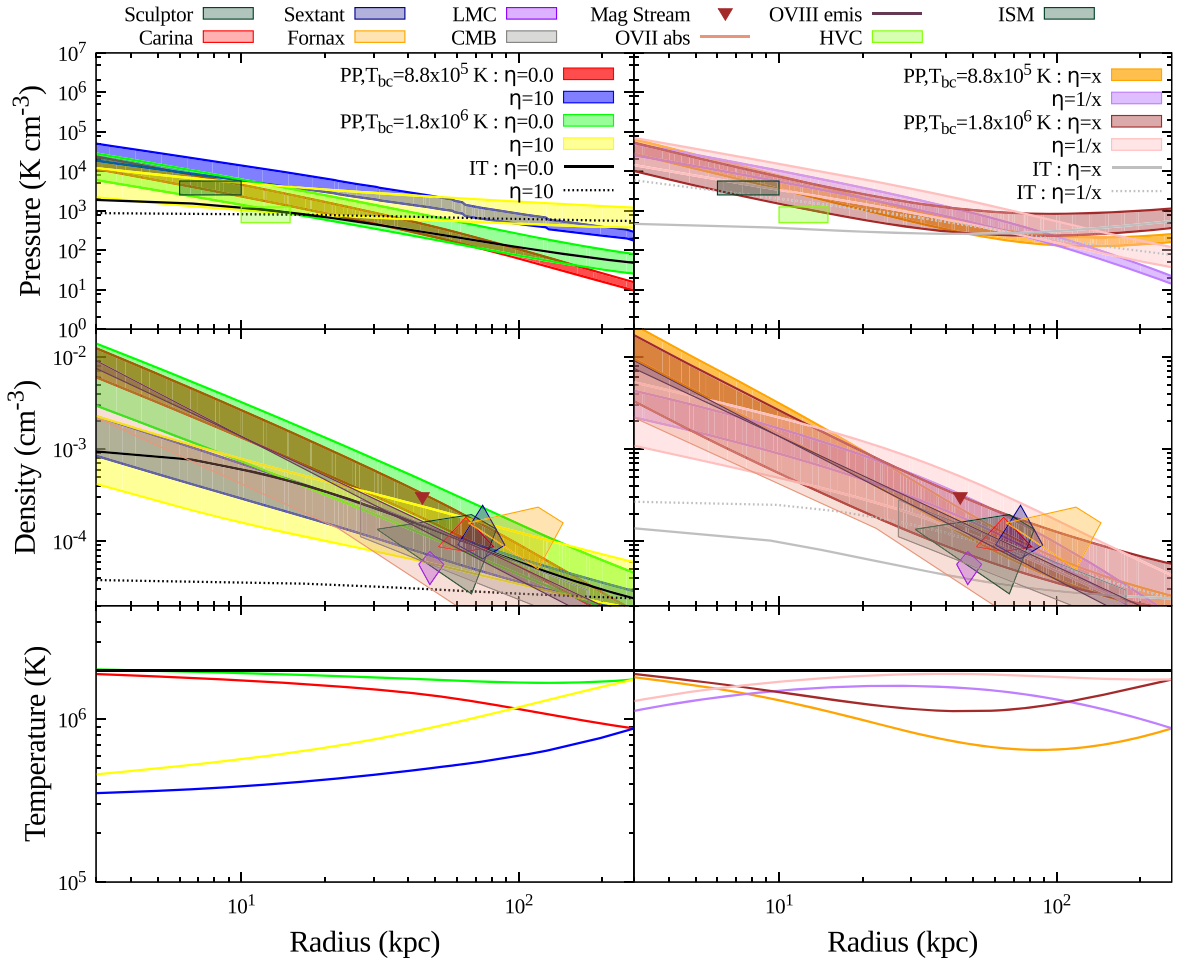

Figure 2. Total pressure (top panel), density (middle panel), and temperature (bottom panel) profiles for different models (IT and PP) without ($\eta = 0$) and with a constant CR population ($\eta = 10$) and the CR profile ($\eta = x$ and $1/x$), where $x = r/r_s$. Different observational constraints of pressure and density are also shown.

and density profiles are shown in green and red for the PP model with no CR component, whereas yellow and blue denote $\eta = 10$ for $T_{\rm bc1}$ and $T_{\rm bc2}$, respectively. In the right panel of Figure 2, the temperature and density profiles are shown in brown and orange for the PP model with $\eta = x$, whereas pink and purple denote $\eta = 1/x$ for $T_{\rm bc1}$ and $T_{\rm bc2}$, respectively.

2.3. Observational Constraints

Figure 2 also shows observational limits on pressure and density from (a) observations of O VII and O VIII (Miller & Bregman 2015); (b) CMB/X-ray stacking (Singh et al. 2018); (c) ram pressure stripping of the LMC (Salem et al. 2015), Carina, Sextans (Gatto et al. 2013), Fornax, and Sculptor (Grcevich & Putman 2009); (d) high-velocity clouds (Putman et al. 2012); (e) the Magellanic Stream (Stanimirović et al. 2002); and (f) interstellar medium pressure (Jenkins & Tripp 2011). We find that the obtained profiles including nonthermal components are within the observational limits. We can also compare the temperature and density profiles with those from simulations that include CRs. In the PP model, the distinguishing feature is a rising temperature profile from the inner to the outer region. CR simulations also show such profiles, e.g., as shown in Figure 5 of Ji et al. (2020), especially beyond the galactocentric radius of ∼10 kpc. This particular profile from Ji et al. (2020) shows a decrease in temperature by a factor ∼7 from the virial radius to ∼10 kpc, similar to that shown in Figure 2 for $\eta = 10$ cases, although the outer boundary temperature is different in the two cases. The difference in the profiles inward of ∼10 kpc is not significant because the difference caused in the column density is small. The curves on the RHS of Figure 2 for declining η cases are similar to the simulation results expected at the outer radii, where PP models predict a declining temperature profile, which is not seen in CR-inclusive simulations. In brief, PP models with constant or declining η profiles appear to capture the CR-simulation temperature and (consequently) density profiles.

2.4. Lognormal Temperature Fluctuation

The observed widths and centroid offsets of O VI absorption lines in the CGM motivate us to consider dynamical disturbances causing temperature fluctuations in the CGM, which results in a multiphase CGM gas. Low-entropy gas parcels uplifted by outflows or high-entropy gas can cool down adiabatically to maintain pressure balance and give rise to temperature and density fluctuations. Turbulence-driven nonlinear oscillations of gravity waves in a gravitationally stratified medium can be an alternative source for these fluctuations. Therefore, we consider an inhomogeneous CGM by including a lognormal temperature distribution (characterized by $\sigma_{\rm lnT}$) around the mean temperature.

Previous studies have considered a lognormal temperature fluctuation for CGM and successfully matched with CGM

observations. Faerman et al. (2017) considered a lognormal distribution for their two-temperature (1.5×10^6 K and 5×10^5 K) CGM model. They found the best-fit value of $\sigma_{\rm lnT}$ to be 0.3 in order to explain the observed O VI column density. We have taken a similar approach. However, we have a single-temperature IT model. Therefore, we consider a lognormal distribution of temperature around the single halo temperature in the case of the IT model. In the case of the PP model, instead of a single temperature, we have a temperature profile $T(r)$. Voit (2019) and Roy et al. (2021) took into account temperature fluctuation in the PP model by considering lognormal distributions with a constant value of $\sigma_{\rm lnT}$ around the mean temperature $T(r)$ at each radius. Voit (2019) found that $\sigma_{\rm lnT} = 0.7$ satisfies the observed O VI column, whereas Roy et al. (2021) concluded a range of $\sigma_{\rm lnT} = 0.6$–1.0 in order to explain the observed O VII, O VIII, and their ratio. In the PP model, we follow a similar approach to that in Voit (2019) and Roy et al. (2021).

3. Results

We calculate the ionization fraction of O VIII using CLOUDY (Ferland et al. 2017) with the input of density and temperature profiles derived from the CGM models. In order to incorporate temperature fluctuation, we calculate the ionization fraction for all the temperatures in a lognormal distribution using CLOUDY and integrate them over the corresponding lognormal distribution to get a mean ionization fraction. That means that for the IT model we get a single mean ionization fraction corresponding to the lognormal distribution around the single temperature of the halo. But for the PP model, we will get mean ionization fractions at each radius corresponding to the lognormal distributions with a constant value of $\sigma_{\rm lnT}$ around the mean temperature $T(r)$ at each radius. We consider two cases: collisional ionization and photoionization along with collisional ionization. We use the extragalactic UV background (Haardt & Madau 2012) at redshift $z = 0$ for photoionization. We take into account our vantage point of observation, i.e., the solar position, and calculate the variation of column density with the Galactic latitude and longitude. We consider the median of the column densities for each value of η in order to compare with the observations.

In Figures 3 (for the IT model) and 4 (for the PP model) we show the variation of $N_{\rm O\ VIII}$ with η, considering collisional ionization (CI) and photoionization (PI) for different models. One can clearly see from these figures that with an increase in η, the value of $N_{\rm O\ VIII}$ decreases owing to the decrease in the temperature. In Figure 3, the brown and blue lines denote the cases with CI and PI, respectively, in the IT model. In this figure, the orange colors denote the effect of lognormal fluctuations ($\sigma_{\rm lnT} = 1.0$). The cases of CI and PI do not differ for $\eta \leqslant 1$, since at $T \sim 10^6$ K CI dominates over PI. However, for $\eta \geqslant 1$, PI leads to slightly larger values of O VIII column density than the CI case, as a further decrease in temperature leads to more production of O VIII by PI. It should be noted that if one considers temperature fluctuation around a single favorable temperature of O VIII, there is less O VIII production with the increase in $\sigma_{\rm lnT}$.

In Figure 4 the orange shaded region indicates the boundary temperature near the virial temperature of the halo 1.8×10^6 K (T_{bc1}) in the PP model, whereas the blue shaded region denotes the boundary condition of 8.8×10^5 K (T_{bc2}) at virial radius. For the PP model, we show the cases with CI without

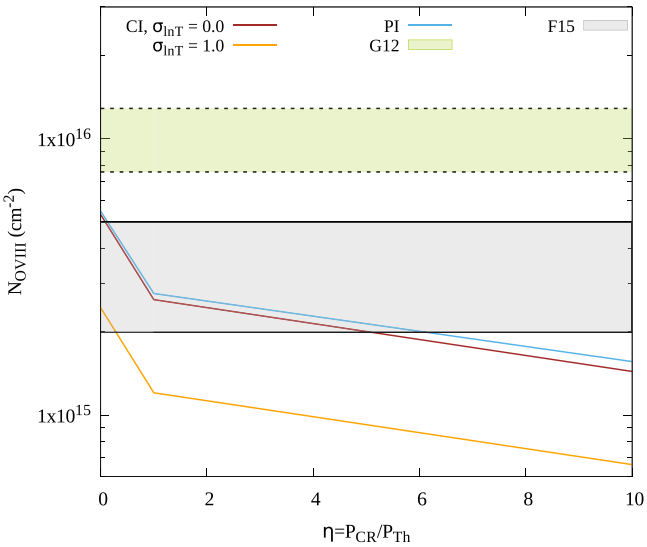

Figure 3. Variation of O VIII column density with η for the IT model with different cases like CI without fluctuation (brown), with fluctuation (orange), and inclusion of PI (blue) with observational constraints by shaded regions from G12 (green) and F15 (gray).

($\sigma_{\rm lnT} = 0.0$) and with fluctuation ($\sigma_{\rm lnT} = 1.0$) and PI in the left, middle, and right panels of Figure 4. The shaded regions in this figure refer to the CGM mass range mentioned earlier in the case of the PP model. A boundary temperature that is close to the favorable temperature for O VIII yields more O VIII than one gets with lower boundary temperatures. However, with the inclusion of temperature fluctuations, one gets almost similar O VIII for both cases. With lower boundary temperature, the production of O VIII decreases for $\eta \geqslant 2$ because the inclusion of η shifts the temperatures from the CI peak of O VIII. However, considering PI in this case can increase the amount of O VIII.

In Figure 5, we show $N_{\rm O\ VIII}$ with different η profiles for both of the models. For the IT model, we use brown and orange colors to denote $\sigma_{\rm lnT} = 0.0$ and 1.0, respectively, whereas circles denote $\eta = x$ and squares denote $\eta = 1/x$. For the PP model, different temperature boundary conditions are shown by orange ($T_{bc} = 1.8 \times 10^6$ K) and red ($T_{bc} = 8.8 \times 10^5$ K) shaded regions, where the shaded region (above the lines for $\eta = x$ and below the lines for $\eta = 1/x$) denotes the mass range for each case in the PP model. One important point to notice here is that declining η profiles produce more O VIII than rising profiles.

3.1. Observations to Compare With

There are some soft X-ray observations of $N_{\rm O\ VIII}$ of the MW by Gupta et al. (2012), Miller & Bregman (2013), and Fang et al. (2015; hereafter referred to as G12, MB13, and F15, respectively). G12 have measured $N_{\rm O\ VIII}$ along eight sight lines with the Chandra telescope. They have quoted the equivalent width (EW) of O VIII instead of $N_{\rm O\ VIII}$ in their paper. However, their measured values of EW of O VIII are increased by 30% for the correction of systematic error, and column densities were therefore recalculated by Faerman et al. (2017). The recalculated values of $\log(N_{\rm O\ VIII})$ are 16.0 (15.88–16.11), respectively. The green shaded regions in Figures 3, 4, and 5 show the ranges of $N_{\rm O\ VIII}$ of G12 as recalculated by Faerman et al. (2017).

O VII lines have been studied by MB13 with XMM-Newton along the 26 sight lines of distant active galactic nuclei

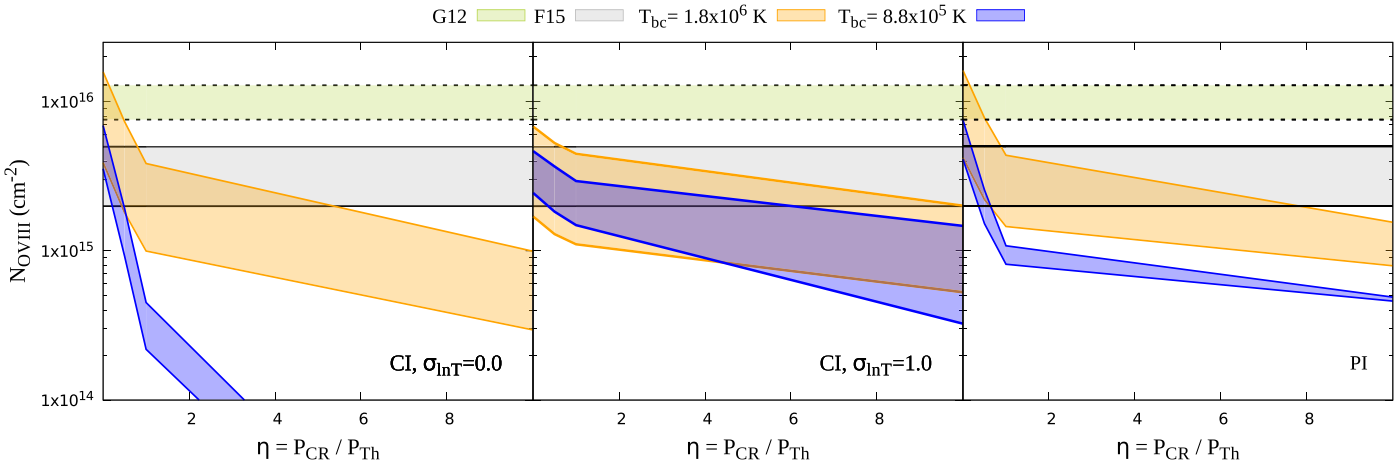

Figure 4. Variation of O VIII column density with η for the PP model with different cases such as CI without fluctuation (left panel), with fluctuation (middle panel), and with PI (right panel). The observational constraints are shown by shaded regions from G12 (green) and F15 (gray). Different temperature boundary conditions are shown by orange ($T_{bc} = 1.8 \times 10^6$ K) and blue ($T_{bc} = 8.8 \times 10^5$ K) shaded regions, where shades denote the mass range for each case.

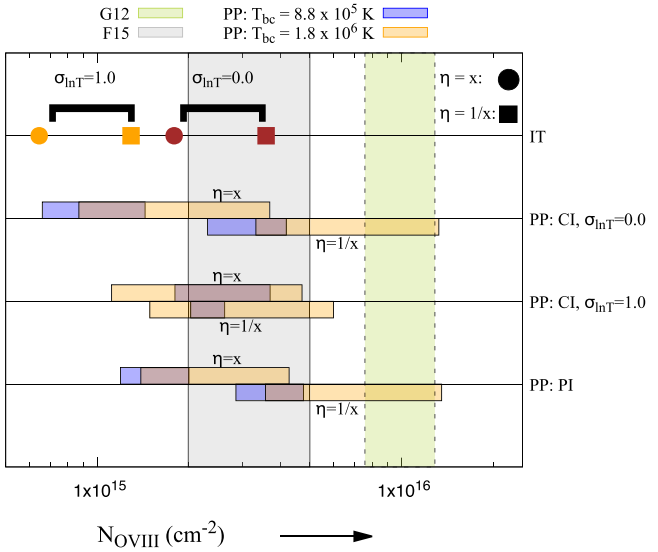

Figure 5. O VIII column density for different η profiles for the IT and PP models with different cases like CI without fluctuation, with fluctuation and inclusion of PI with observational constraints by shaded regions from G12 (green) and F15 (gray). Different temperature boundary conditions are shown by orange ($T_{bc} = 1.8 \times 10^6$ K) and blue ($T_{bc} = 8.8 \times 10^5$ K) shaded regions, where the shaded region (above the lines for $\eta = x$ and below the lines for $\eta = 1/x$) denotes the mass range for each case in the PP model. For the IT model, brown and orange colors are used to denote $\sigma_{\rm lnT} = 0.0$ and 1.0, respectively, whereas circles denote $\eta = x$ and squares denote $\eta = 1/x$.

(AGNs), as well as only one detection of O VIII with a ratio of $N_{\rm O\ VII}/N_{\rm O\ VIII} = 0.7 \pm 0.2$. F15 observed the O VII absorption line for a broader sample of 43 AGNs, which includes the sample from MB13. They reported a wider range of $N_{\rm O\ VII}$ ($10^{15.5}$–$10^{16.5}$ cm^{-2}), with the central value at 10^{16} cm^{-2}. However, they have arrived at these values by setting aside the nondetection along 10 sight lines. Adding these upper limits to the detected sample, Faerman et al. (2017) have come up with a new range of values of log($N_{\rm O\ VII}$): 16.15 (16.0–16.3). Although F15 did not report O VIII lines, Faerman et al. (2017) calculated the median of the ratio of $N_{\rm O\ VII}$ and $N_{\rm O\ VIII}$ from G12 observations. Using this ratio and the recalculated value of $N_{\rm O\ VII}$ from F15, they calculate log($N_{\rm O\ VIII}$), which ranges from 15.3 to 15.7 with a median value of 15.5. The gray shaded regions in Figures 3, 4, and 5 show the ranges of $N_{\rm O\ VII}$ and $N_{\rm O\ VIII}$ of F15 as recalculated by Faerman et al. (2017). Note that these rederived ranges of $N_{\rm O\ VIII}$ indicate 1σ uncertainty around the median value.

Table 1
Constraints of η on the Basis of $N_{\rm O\ VIII}$ Observations by G12 and F15

Model		CI (without Fluctuations)		CI (with Fluctuations)		PI	
		G12	F15	G12	F15	G12	F15
PP	T_{bc1}	0.5	6	⋯	10	0.5	8
	T_{bc2}	⋯	0.5	⋯	6	⋯	1
IT		⋯	5	⋯	1	⋯	6

3.2. Constraints

We have tabulated the constraints on η for different models in Table 1. It is evident from Figures 3, 4, and 5 that $N_{\rm O\ VIII}$ can help in putting upper limits on η. For the IT model, we find that $\eta \leqslant 5$ if one considers only CI with no temperature fluctuations. The inclusion of PI slightly changes this constraint to $\eta \leqslant 6$. We can also clearly see that introducing lognormal fluctuations makes these constraints even stronger ($\eta \leqslant 1$; Figure 3). Interestingly, we find that the models with varying η with radius can be accommodated within observational limits by suitably decreasing $\sigma_{\rm lnT}$ (Figure 5). For example, in Figure 5, the model of increasing η with radius for $\sigma_{\rm lnT} = 0$ is fairly close to the bottom range of F15's data, and for the opposite case ($\eta = 1/x$), decreasing $\sigma_{\rm lnT}$ sufficiently can put it in the ballpark of F15's data.

A larger upper limit ($\eta \leqslant 8$) is allowed for the case of the PP model with $T_{\rm bc1}$ if one considers observations of F15. In general, we find that the inclusion of temperature fluctuation relaxes these limits in all the cases by allowing a larger value of η ($\leqslant$10) (Figure 4). Furthermore, spatial variation of η (Figure 5) can be allowed within the observational limits by increasing temperature fluctuations and using a suitable mass range in the PP model. In particular, models with a declining ratio of CR to thermal pressure with radius (as hinted in the simulations of, e.g., Butsky & Quinn 2018) predict O VIII column densities within observational limits. Note that, in the PP case, the requirement for $\sigma_{\rm lnT}$ for varying η models runs

opposite to that in the IT case, where varying η models require smaller $\sigma_{\ln T}$ in order to be viable.

To see the effect of normalization for the cases $\eta = Ax$ and $\eta = A/x$, we have increased the value of A, which increases the CR pressure. This leads to a decrease in the density or temperature, or both, and consequently decreases the O VIII column density. Therefore, all the plots in Figure 5 will shift toward the left with the increment of the normalization. This implies that $\eta = A \times x$ cases are not allowed for both IT and PP models even with the inclusion of photoionization and temperature fluctuations. However, in the case of the PP model, for $\eta = A/x$ with $A \geqslant 1$, all the cases do not satisfy the observational constraints except for the case with boundary temperature 1.8×10^6 K, for $A \leqslant 10$. On the other hand, in the case of IT, for the $\eta = A/x$ profiles, the O VIII column densities are within the observational constraints for the cases $A \leqslant 8$. This implies that these models allow the central region to have a large CR pressure of even $\eta = 200$, but not in the outer halo. This result differs from the findings by previous simulations that show a CR-dominated outer halo (Butsky & Quinn 2018). As the normalization increment shifts all the plots toward left, the inclusion of temperature fluctuations is ruled out for the models with $\eta = A/x$ profiles except for a very small range with high CGM mass in the PP model with boundary temperature 1.8×10^6 K and $A \leqslant 2$.

4. Discussion

Our constraints allow larger values of η for most of the cases in comparison to the isentropic model by Faerman et al. (2020, 2022). In their recent work (Faerman et al. 2022), they have considered three cases for their model: (1) with only thermal pressure, i.e., $\alpha = (P_{nth}/P_{th}) + 1.0 = ((P_{CR} + P_B)/P_{th}) + 1.0 = 1.1$; (2) with the standard case as considered in Faerman et al. (2020), i.e., $\alpha = 2.1$; and (3) with significant nonthermal pressure where $\alpha = 2.9$. Note that the above-mentioned values of α are the values at the outer boundary and the profiles of α will follow a declining pattern as radius decreases (see the blue curve in the right panel of Figure 2 in Faerman et al. 2020). With our definition of η, along with the magnetic field value used by us, we can convert these α values to $\eta \sim 0$, 0.6, and 1.4, respectively, for their three cases. The thermal case matches $N_{\rm O\ VIII}$ observations up to a CGM mass of $10^{11}\ M_\odot$, and for the standard case, the value of $N_{\rm O\ VIII}$ is comparable to the observed value. However, for the significant nonthermal case, the O VIII value is lower than the observations by a factor of $\sim$10 for a CGM mass of $10^{11}\ M_\odot$. Therefore, one can say that $\eta < 0.6$ is allowed for the isentropic model. For the PP model, we get an upper limit of $\eta \sim 0.5$ for the two cases, which are therefore in agreement with the constraint from the isentropic model. However, for most of our models, the upper limits derived in the present work are larger than the isentropic model.

It should be noted that the limits of η derived here translate to constraints on CR pressure in the hot diffuse CGM, and one may wonder about the CR pressure in the cold gas. CR pressure scales with the density ($P_{CR} \propto \rho^{\gamma_{c,\rm eff}}$, where $\gamma_{c,\rm eff}$ is the effective adiabatic index of the CR) of the gas; where the adiabatic index depends on the transport mechanism (Butsky et al. 2020), the limits of CR pressure in the cold gas would be different from what we have found for the hot gas. If CRs are strongly coupled to the gas, then in the limit of slow CR transport, i.e, if the only CR transport mechanism is advection, $\gamma_{c,\rm eff} = \gamma_c = 4/3$. In this case, CR pressure can be higher in cooler, denser gas than in the hot gas. However, in the limit of efficient CR transport, i.e., if there is CR diffusion, streaming along with advection, the CR pressure will be redistributed from a high-density, cold region to a diffuse, hot region of the CGM, which will lower the $\gamma_{c,\rm eff}$. In this limit, $\gamma_{c,\rm eff} \to 0$, and the limits of CR pressure in the cold phase are nearly equal to the CR pressure in the hot phase. In the context of a single phase temperature with temperature gradient, if one considers CR pressure in the hot phase to scale as $\rho_g^{\gamma_{c,\rm eff}}$, then η is proportional to $\rho_g^{\gamma_{c,\rm eff}-(5/3)}$, as the adiabatic index for gas is $5/3$. Then, η will be proportional to $\rho_g^{-1/3}$ and $\rho_g^{-5/3}$, respectively, depending on slow and effective transport mechanism. This implies that η is smaller in denser gas and hence mimics a rising profile of η in the case of the single hot-phase gas, which we have shown in the present paper.

However, these scaling relations are for adiabatic situations, which is not the case for the PP model, which involves energy loss. In the context of cold gas that may have condensed out of the hot gas, it is possible for the cold gas to contain a significant amount of CR pressure, with a large value of η for cold gas. Simulations by Butsky et al. (2020, their Figure 10) showed that in the limit of slow CR transport the value of η is quite different for hot and cold gas. In the limit of efficient transport, CR pressure is decoupled from the gas, and η has similar values in hot and cold gas. If we recall the observation by Werk et al. (2014) that the cold phase of the CGM nearly follows the hot gas density profile, then for small density contrast the CR pressure in the cold phase and hot phase may not differ much even with different transport mechanisms. But even with small density contrast, thermal pressure of cold gas will be smaller than hot phase by two orders of magnitude owing to the temperature difference, which allows for a larger upper limit on η. However, packing more CRs in cold gas will not have any effect on the constraints derived here. In fact, this may be one way to circumvent the constraints described here.

We have not included any disk component in the present work. A recent work by Kaaret et al. (2020) took into account an empirical disk density profile motivated by the measured molecular profile of the MW along with the halo component. They pointed out that the high-density disk model can well fit the MW's soft X-ray emission, whereas it underpredicts the absorption columns. Their conclusion is that the dominant contribution of X-ray absorption comes from the halo component owing to large path length. In addition, this difference in contribution comes from the fact that the absorption is proportional to density, whereas emission measure is proportional to density squared. Therefore, considering only the halo component and making the comparison with the absorption column is justified.

Note that the limits derived here are sensitive to some of the parameters, such as the magnetic field and metallicity. An increase (decrease) in the magnetic pressure would increase (decrease) the total nonthermal pressure, which would decrease (increase) the limit on η. However, given the uncertainty in the magnetic field strength in the CGM, equipartition of magnetic energy with thermal energy is a reasonable assumption. For a collisionally ionized plasma, which we assume for the CGM gas, the column density is proportional to the metallicity (Z) in the case of the IT model, whereas it is proportional to $Z^{0.3}$ for the PP model (see Equation (17) of Voit 2019). In the photoionized case, the dependence on metallicity will be

stronger since the ion abundance would also depend on the metallicity. Also note that the limits derived here refer to the CR population spread extensively in the CGM. A localized but significant CR population may elude the above limits. However, we also note that most of the contribution of the limits comes from the inner region, where O VIII exists otherwise and is suppressed owing to CRs. Therefore, our limits also pertain to localized CR populations in the inner regions.

5. Summary

We have studied two analytical models of the CGM (IT and PP) in hydrostatic equilibrium in light of the observations of $N_{\rm O\ VIII}$ in order to constrain the CR population in the MW CGM. We found that $\eta \leqslant 10$ in the case of no photoionization and including temperature fluctuations in the PP model, whereas the IT model allows $\eta \leqslant 6$ with inclusion of PI. However, it should be noted that IT is an extremely simplistic model and the inclusion of a nonthermal component leads to a very low density. The limits from IT may therefore be only of academic interest.

Combined with the limits derived from the γ-ray background (Jana et al. 2020), our results make it difficult for a significant CR population in the MW. However, models in which the ratio of CR to thermal pressure varies with radius (preferably declining with radius) can be accommodated within observational constraints, if they include suitable temperature fluctuation (larger $\sigma_{\rm lnT}$ for PP and lower for IT), although making allowances for large values of η only in the central region.

ORCID iDs

Manami Roy https://orcid.org/0000-0001-9567-8807
Biman B. Nath https://orcid.org/0000-0003-1922-9406

References

Anderson, M. E., Churazov, E., & Bregman, J. N. 2015, MNRAS, 452, 3905
Bernet, M. L., Miniati, F., Lilly, S. J., Kronberg, P. P., & Dessauges-Zavadsky, M. 2008, Natur, 454, 302
Butsky, I. S., Fielding, D. B., Hayward, C. C., et al. 2020, ApJ, 903, 77
Butsky, I. S., & Quinn, T. R. 2018, ApJ, 868, 108
Cai, Z., Fan, X., Bian, F., et al. 2017, ApJ, 839, 131
Dashyan, G., & Dubois, Y. 2020, A&A, 638, A123
Faerman, Y., Pandya, V., Somerville, R. S., & Sternberg, A. 2022, ApJ, 928, 37
Faerman, Y., Sternberg, A., & McKee, C. F. 2017, ApJ, 835, 52
Faerman, Y., Sternberg, A., & McKee, C. F. 2020, ApJ, 893, 82
Fang, T., Buote, D., Bullock, J., & Ma, R. 2015, ApJS, 217, 21
Ferland, G. J., Chatzikos, M., Guzmán, F., et al. 2017, RMxAA, 53, 385
Gatto, A., Fraternali, F., Read, J. I., et al. 2013, MNRAS, 433, 2749
Grcevich, J., & Putman, M. E. 2009, ApJ, 696, 385
Gupta, A., Mathur, S., Krongold, Y., Nicastro, F., & Galeazzi, M. 2012, ApJL, 756, L8
Haardt, F., & Madau, P. 2012, ApJ, 746, 125
Henley, D. B., & Shelton, R. L. 2010, ApJS, 187, 388
Henley, D. B., Shelton, R. L., Kwak, K., Joung, M. R., & Mac Low, M.-M. 2010, ApJ, 723, 935
Hennawi, J. F., Prochaska, J. X., Cantalupo, S., & Arrigoni-Battaia, F. 2015, Sci, 348, 779
Hummels, C. B., Smith, B. D., Hopkins, P. F., et al. 2019, ApJ, 882, 156
Jana, R., Roy, M., & Nath, B. B. 2020, ApJL, 903, L9
Jenkins, E. B., & Tripp, T. M. 2011, ApJ, 734, 65
Ji, S., Chan, T. K., Hummels, C. B., et al. 2020, MNRAS, 496, 4221
Ji, S., Oh, S. P., & McCourt, M. 2018, MNRAS, 476, 852
Kaaret, P., Koutroumpa, D., Kuntz, K. D., et al. 2020, NatAs, 4, 1072
Kim, J., Golwala, S., Bartlett, J. G., et al. 2022, ApJ, 926, 179
Lan, T.-W., & Prochaska, J. X. 2020, MNRAS, 496, 3142
Li, Y., Bryan, G. L., Ruszkowski, M., et al. 2015, ApJ, 811, 73
McCourt, M., O'Leary, R. M., Madigan, A.-M., & Quataert, E. 2015, MNRAS, 449, 2
McCourt, M., Sharma, P., Quataert, E., & Parrish, I. J. 2012, MNRAS, 419, 3319
Miller, M. J., & Bregman, J. N. 2013, ApJ, 770, 118
Miller, M. J., & Bregman, J. N. 2015, ApJ, 800, 14
Navarro, J. F., Frenk, C. S., & White, S. D. M. 1996, ApJ, 462, 563
Peeples, M. S., Corlies, L., Tumlinson, J., et al. 2019, ApJ, 873, 129
Planck Collaboration, Ade, P. A. R., Aghanim, N., et al. 2013, A&A, 557, A52
Prochaska, J. X., Macquart, J.-P., McQuinn, M., et al. 2019, Sci, 366, 231
Prochaska, J. X., Werk, J. K., Worseck, G., et al. 2017, ApJ, 837, 169
Putman, M. E., Peek, J. E. G., & Joung, M. R. 2012, ARA&A, 50, 491
Roy, M., Nath, B. B., & Voit, G. M. 2021, MNRAS, 507, 3849
Ruszkowski, M., Yang, H.-Y. K., & Reynolds, C. S. 2017, ApJ, 844, 13
Salem, M., Bryan, G. L., & Corlies, L. 2015, MNRAS, 456, 582
Sharma, P., McCourt, M., Quataert, E., & Parrish, I. J. 2012, MNRAS, 420, 3174
Singh, P., Majumdar, S., Nath, B. B., & Silk, J. 2018, MNRAS, 478, 2909
Stanimirović, S., Dickey, J. M., Krčo, M., & Brooks, A. M. 2002, ApJ, 576, 773
Stocke, J. T., Keeney, B. A., Danforth, C. W., et al. 2013, ApJ, 763, 148
Tumlinson, J., Peeples, M. S., & Werk, J. K. 2017, ARA&A, 55, 389
van de Voort, F., Springel, V., Mandelker, N., van den Bosch, F. C., & Pakmor, R. 2019, MNRAS, 482, L85
Voit, G. M. 2019, ApJ, 880, 139
Voit, G. M., & Donahue, M. 2015, ApJL, 799, L1
Werk, J. K., Prochaska, J. X., Cantalupo, S., et al. 2016, ApJ, 833, 54
Werk, J. K., Prochaska, J. X., Tumlinson, J., et al. 2014, ApJ, 792, 8
Wiener, J., Pfrommer, C., & Oh, S. P. 2017, MNRAS, 467, 906
Wiener, J., Zweibel, E., & Oh, P. 2013, ApJ, 767, 87
Zhang, D. 2018, Galax, 6, 114